Zitierweise: *Angew. Chem. Int. Ed.* **2024**, *63*, e202409019
doi.org/10.1002/anie.202409019

Electrocatalysis

Efficient Electrosynthesis of Urea over Single-Atom Alloy with Electronic Metal Support Interaction

Peng Zhan, Jinjie Zhuang, Shuai Yang, Xuechun Li, Xuehan Chen, Tian Wen, Lu Lu, Peiyong Qin,* and Buxing Han**

Abstract: Urea electrosynthesis from carbon dioxide (CO_2) and nitrate (NO_3^-) is an alternative approach to traditional energy-intensive urea synthesis technology. Herein, we report a CuAu single-atom alloy (SAA) with electronic metal support interaction (EMSI), achieving a high urea yield rate of 813.6 $\mu g\,h^{-1}\,mg_{cat}^{-1}$ at −0.94 V versus reversible hydrogen electrode (vs. RHE) and a Faradaic efficiency (FE) of 45.2 % at −0.74 V vs. RHE. In situ experiments and theoretical calculations demonstrated that single-atom Cu sites modulate the adsorption behavior of intermediate species. Bimetallic sites synergistically accelerate C–N bond formation through spontaneous coupling of *CO and *NO to form *ONCO as key intermediates. More importantly, electronic metal support interaction between CuAu SAA and CeO_2 carrier further modulates electron structure and interfacial microenvironment, endowing electrocatalysts with superior activity and durability. This work constructs SAA electrocatalysts with EMSI effect to tailor C–N coupling at the atomic level, which can provide guidance for the development of C–N coupling systems.

Introduction

Urea ($CO(NH_2)_2$), the main component of nitrogen fertilizer, is an indispensable nourishment in agricultural fields for human society.[1,2] At present, urea industrial production is conducted under high temperature and pressure, consuming massive amounts of fossil energy and releasing excess greenhouse gases.[3] Compared with traditional industrial methods, electrochemical methods can generate urea directly with renewable electricity under mild conditions, which has been considered as a promising approach to resolve the looming energy and environmental crises.

Recent advances demonstrate urea electrosynthesis by coupling carbon dioxide (CO_2) and nitrate (NO_3^-) provides an intriguing approach for direct urea production. Various electrocatalysts have been reported. For instance, Fe–Ni pairs act as efficient electrocatalysts for urea synthesis, achieving a urea yield rate of 1212 $\mu g\,h^{-1}\,mg_{cat}^{-1}$ with a corresponding Faradaic efficiency (FE) of 17.8 %.[4] In-$(OH)_3$-S with well-defined (100) facets can enhance the coupling of $*NO_2$ and $*CO_2$ directly with a urea yield rate of 533.1 $\mu g\,h^{-1}\,mg_{cat}^{-1}$ and a urea FE of 53.4 %,[5] Core-shell Cu@Zn nanowires can promote urea synthesis with a yield rate of 556.8 $\mu g\,h^{-1}\,mg_{cat}^{-1}$ and a urea FE of 7.3 %.[6] Besides, $CuWO_4$,[7] Bi_2Se_3 nanosheets,[8] Cu with an atomic-scale spacing,[9] and MoO_x/C[10] have also been developed for electrochemical synthesis of urea from CO_2 and NO_3^-. Although great efforts have been made, urea electrochemical synthesis still suffers from predicaments of inescapable by-products, mainly produced by parallel CO_2 reduction reaction (CO_2RR), NO_3^- reduction reaction (NO_3RR), and hydrogen evolution reaction (HER). Electrocatalyst design with high activity and selectivity is of great significance yet challenging.

Supported metal catalysts have been widely applied in the field of heterogeneous catalysis. Catalytic properties of supported metal catalysts might be affected by electronic perturbations due to electronic metal support interaction (EMSI), formally put forward by C.T. Campbell in 2012.[11] EMSI has been considered as the interaction between metal and transition-metal oxide (e.g. CeO_2, TiO_2), which can tailor microenvironments via electron transfer and coordination structure design, thus directly enhancing intrinsic catalytic activities. However, little attention has been paid to taking advantage of EMSI effect for enhancing the electrochemical coupling of CO_2 and NO_3^-. The design of metal-

[*] P. Zhan, S. Yang, Prof. P. Qin
National Energy R&D Center for Biorefinery, Beijing University of Chemical Technology
Beijing, 100029 (China)
E-mail: qinpy@mail.buct.edu.cn

J. Zhuang, X. Chen, T. Wen, Dr. L. Lu
Paris Curie Engineer School, Beijing University of Chemical Technology
Beijing, 100029 (China)
E-mail: lulu2015@iccas.ac.cn

Prof. B. Han
Beijing National Laboratory for Molecular Sciences, CAS Key Laboratory of Colloid and Interface and Thermodynamics, CAS Research, Education Center for Excellence in Molecular Sciences, Center of Carbon Neutral Chemistry, Institute of Chemistry, Chinese Academy of Sciences
Beijing, 100029 (China)
E-mail: hanbx@iccas.ac.cn

X. Li
College of Chemistry, Beijing University of Chemical Technology
Beijing, 100029 (China)

© 2024 Wiley-VCH GmbH

based catalysts with EMSI effect for selective urea electrosynthesis deserves more research.

Single-atom alloys (SAAs), in which one of the active metals is atomically dispersed onto the surface of another host metal, combining advantages of bimetallic alloys and single atoms, have gained ever-rising attention in electrocatalytic reactions.[12] Its unique electronic structures and strong bimetallic synergy effects show potentials in breaking linear scaling relationships, promoting activities and selectivity in heterogeneous catalysis.[13–15] Besides, metal-metal bonds and coordination structures in SAAs can modulate reaction intermediates and reaction pathways. The exploration of transition-metal oxide supported SAAs with EMSI effect endows enormous opportunities to achieve performance augment for urea electrosynthesis.

In this work, we design CuAu single-atom alloy (SAA) on CeO_2 nanorods with EMSI effect to serve as efficient electrocatalysts toward urea synthesis by coupling CO_2 and NO_3^-. Systematic characterizations clearly reveal the existence of EMSI between CuAu SAA and CeO_2 support. The resultant $Cu_1Au_8@CeO_2$ electrocatalyst has superior urea selectivity with a Faradaic efficiency (FE) of 45.2 % at −0.74 V vs. RHE, achieving a urea yield rate of 813.6 $\mu g\,h^{-1}\,mg_{cat}^{-1}$ at −0.94 V vs. RHE. Furthermore, in situ experiments and theoretical calculations indicate Cu–Au dual sites enhance C–N bond formation through spontaneous coupling of *CO and *NO to generate the key *ONCO intermediate for urea synthesis. Single-atom Cu sites further regulate adsorption behaviors of intermediate species. More importantly, EMSI between CuAu SAA and CeO_2 modulates electron structure and interfacial environment, endowing electrocatalysts with superior activity and durability. This work constructs SAA electrocatalysts and further utilizes EMSI to enhance urea synthesis.

Results and Discussion

The synthesis process is described in Figure S1. The contents of Cu and Au in electrocatalysts were measured by inductively coupled plasma atomic emission spectroscopy (ICP-AES), revealing concentrations of 0.9 % for Cu and 7.3 % for Au, respectively. The obtained electrocatalyst was denoted as $Cu_1Au_8@CeO_2$. $Cu_1Au_8@CeO_2$ was then characterized in detail. Transmission electron microscopy (TEM) image of $Cu_1Au_8@CeO_2$ in Figure 1a displays CuAu SAA nanoparticles (NPs) loaded onto CeO_2 nanorods. Meanwhile, $Cu@CeO_2$, $Au@CeO_2$, and CeO_2 were prepared as reference samples, their TEM images are shown in Figure S2. Aberration-corrected high-angle annular dark-field scanning transmission electron microscopy (HAADF-STEM) image (Figure 1b) of $Cu_1Au_8@CeO_2$ further validates CuAu SAA with an average size of ~5 nm is well-anchored onto CeO_2. The lattice spacing of 0.326 nm corresponds to (111) planes of CeO_2, and 0.203 nm and 0.235 nm associated with (200) and (111) planes of Au respectively.[16,17] Corresponding selected-area electron diffraction (SAED) pattern (Figure S3) can be indexed to crystal planes of Au, implying single-atom Cu sites are highly disperse over $Cu_1Au_8@CeO_2$. Randomly magnified image indicates atomically dispersed Cu sites (marked by yellow circles, Figure 1c) are isolated by surrounding Au atoms, which is originated from Au NPs with atomic vacancies formed by bonding with neighboring Cu atoms. Corresponding energy-dispersive spectroscopic (EDS) elemental mappings in Figure 1d-1 g illustrate a uniform distribution of Cu and Au over CeO_2. To investigate the presence of oxygen vacancies (V_O) in CeO_2, electron paramagnetic resonance (EPR) spectroscopy is conducted (Figure 1h), and EPR signal at $g = 2.0397$ indicates the presence of unpaired electrons, confirming the existence of oxygen vacancies in $Cu_1Au_8@CeO_2$.[18]

X-ray diffraction (XRD) was performed to investigate phase structures of electrocatalysts in Figure 1i. The peaks of Au (111) in $Au@CeO_2$ and $Cu_1Au_8@CeO_2$ are slightly shifted compared with the standard Au (JCPDS#04–0784), it further confirms EMSI effect between metal components and CeO_2. No diffraction peaks of Cu or CuO can be found in $Cu_1Au_8@CeO_2$, implying a high dispersion degree of Cu species. X-ray photoelectron spectroscopy (XPS) was employed to determine surface chemical statuses of $Cu_1Au_8@CeO_2$ and $Au@CeO_2$ in Figure 1j–k and Figure S4–S5. As displayed in Figure 1j, Cu 2p signals can be observed at 953.6, 934.5, and 933.3 eV, corresponding to Cu $2p_{1/2}$ and Cu $2p_{3/2}$,[19] while Au 4f peaks locate at 86.7 eV and 82.7 eV for Au $4f_{5/2}$ and Au $4f_{7/2}$ respectively. Compared to the binding energy of Au $4f_{5/2}$ (86.5 eV) and Au $4f_{7/2}$ (82.7 eV) in $Au@CeO_2$, the binding energy of Au in $Cu_1Au_8@CeO_2$ shift slightly, ascribed to electronic interaction and charge transfer between Au and Cu. Ultraviolet photoelectron spectroscopy (UPS) was conducted to identify interactions between metal components and CeO_2 by evaluating work function (WF) via the $E_{cut\text{-}off}$[20] (Figure 1I). WFs of $Au@CeO_2$ and $Cu_1Au_8@CeO_2$ were estimated to be 6.72 eV and 3.65 eV respectively. A smaller WF of $Cu_1Au_8@CeO_2$ indicates higher mobility and a lower hurdle for electrons to participate in surface reactions,[21] suggesting single-atom Cu sites can enhance EMSI effect between SAA and CeO_2. Surface areas and porosity properties of these electrocatalysts were investigated by Brunauer–Emmett–Teller (BET) analysis (Figure S6). Resulting BET plots reveal specific surface areas of 135.23 $m^2\,g^{-1}$, 140.51 $m^2\,g^{-1}$ and 127.44 $m^2\,g^{-1}$ for $Cu_1Au_8@CeO_2$, $Au@CeO_2$, and CeO_2, respectively. The increase in specific surface areas can be attributed to well-dispersed Cu_1Au_8 SAA NPs anchored onto CeO_2 nanorods.

Valence states and coordination configurations of Cu and Au sites in $Cu_1Au_8@CeO_2$ are further validated by synchrotron-based X-ray absorption spectroscopy (XAS). X-ray absorption near-edge structure (XANES) and extended X-ray absorption fine structure (EXAFS) provide a more detailed understanding of metal atoms. In the XANES spectra of $Cu_1Au_8@CeO_2$, the near-edge absorption of the Cu K-edge (Figure 2a) exhibits a distinct energy absorption edge profile in comparison with Cu foil, confirming charge polarization between adjacent Cu atoms and Au atoms. The modified electronic properties of Cu atoms are expected to facilitate C–N coupling and modulate binding strength of

 © 2024 Wiley-VCH GmbH

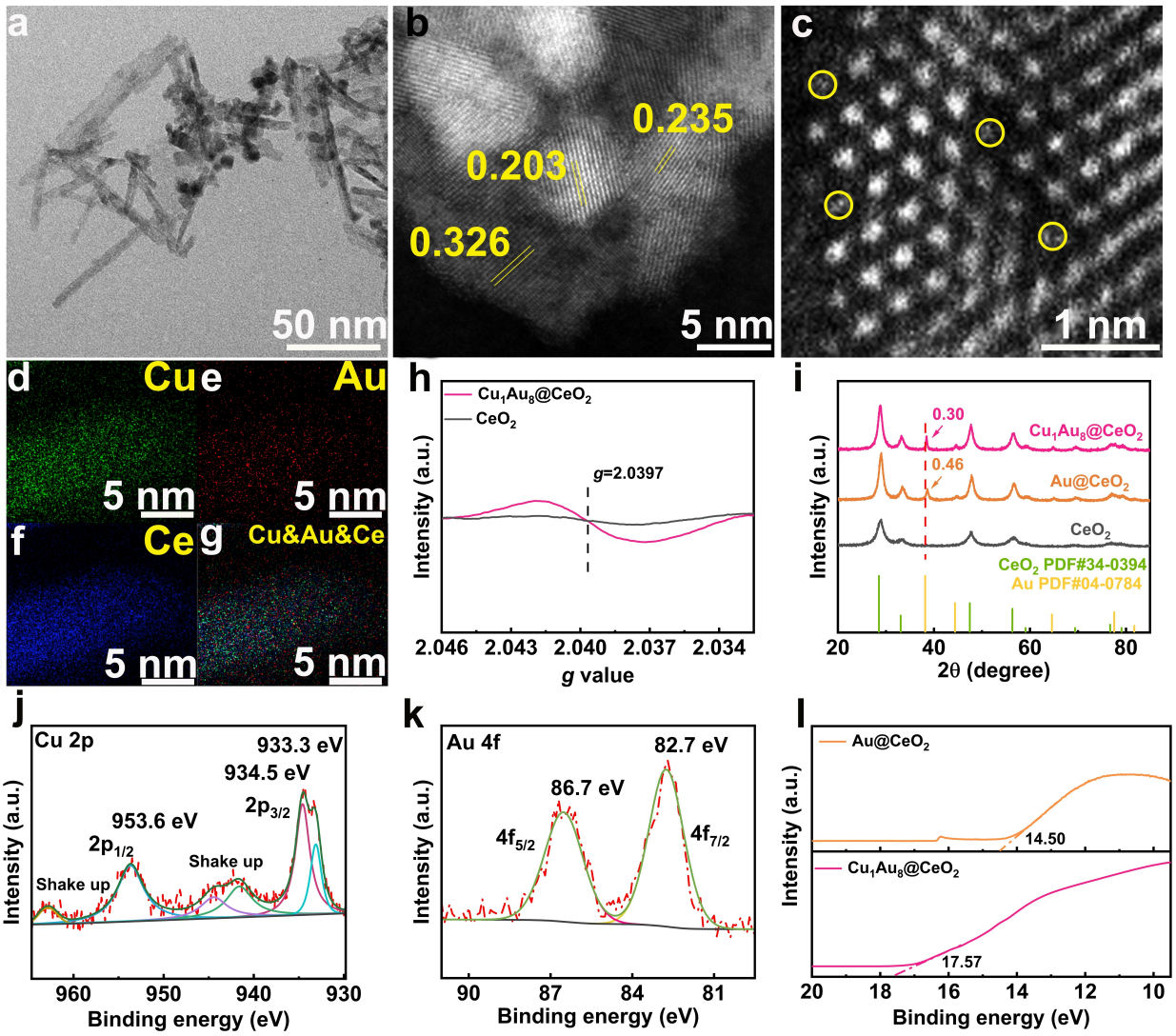

Figure 1. a) Transmission electron microscopy image of $Cu_1Au_8@CeO_2$. b,c) Aberration-corrected high-angle annular dark-field scanning transmission electron microscopy images of $Cu_1Au_8@CeO_2$. d–g) Corresponding energy-dispersive spectroscopic elemental mappings for Cu, Au, Ce, and all of them in $Cu_1Au_8@CeO_2$. h) Electron paramagnetic resonance spectroscopy of $Cu_1Au_8@CeO_2$, $Au@CeO_2$, and CeO_2. i) X-ray diffraction patterns of $Cu_1Au_8@CeO_2$, $Au@CeO_2$ and CeO_2. j,k) X-ray photoelectron spectroscopy spectra of $Cu_1Au_8@CeO_2$. l) Ultraviolet photoelectron spectroscopy images of $Cu_1Au_8@CeO_2$ and $Au@CeO_2$.

adsorbed intermediates, thus endowing $Cu_1Au_8@CeO_2$ with remarkable electrocatalytic activity. According to Fourier transformed (FT) k^3-weighted EXAFS spectra of Cu K-edge for $Cu_1Au_8@CeO_2$ in Figure 2b, the dominant peak in the first coordinated shells (1.50 Å) upon R-space curve of Cu K-edge originating from the scattering of the first shell Cu–O path, is almost the same in the position as that of CuO, indicating an identical coordination environment for Cu atoms in $Cu_1Au_8@CeO_2$. Moreover, the second coordination shell of $Cu_1Au_8@CeO_2$ splits into two peaks (2.24 Å and 2.80 Å), apparently distinct from Cu foil and CuO, due to the effect of backscattering of neighboring Au atoms.[22] In the Au L_3-edge XANES spectra (Figure 2c), it is manifest that white line peak of Au in $Cu_1Au_8@CeO_2$ situates at higher energy than that of Au foil, which indicates electron transfers from Au atoms to surrounding CeO_2 and single-atom Cu, validating EMSI effect in $Cu_1Au_8@CeO_2$. Fourier transformation of Au L_3-edge spectra is illustrated in Figure 2d. Au–O path (1.60 Å) verifies bonds between Au and CeO_2. In contrast to Au foil, $Cu_1Au_8@CeO_2$ sample indicates distinct peaks of Au–Au, suggesting electronic interactions between Au and Cu sites. Wavelet transform (WT)-EXAFS was also conducted to identify Cu–O and Cu-metal paths in Cu foil, CuO and $Cu_1Au_8@CeO_2$ (Figure 2g–i), further confirming atomically dispersed Cu sites. Based on the fitting results (Figure 2e–f), the coordination number (CN) of Cu–O, Cu–Au1, and Cu–Au2 were estimated to be 4.0, 6.0 and 4.0 respectively (Table S1). Therefore, these detailed characterizations demonstrate the formation of CuAu SAA and EMSI effect between SAA and CeO_2.

Electrochemical measurements were carried out in a H-type configuration with three electrodes. Linear sweep

© 2024 Wiley-VCH GmbH

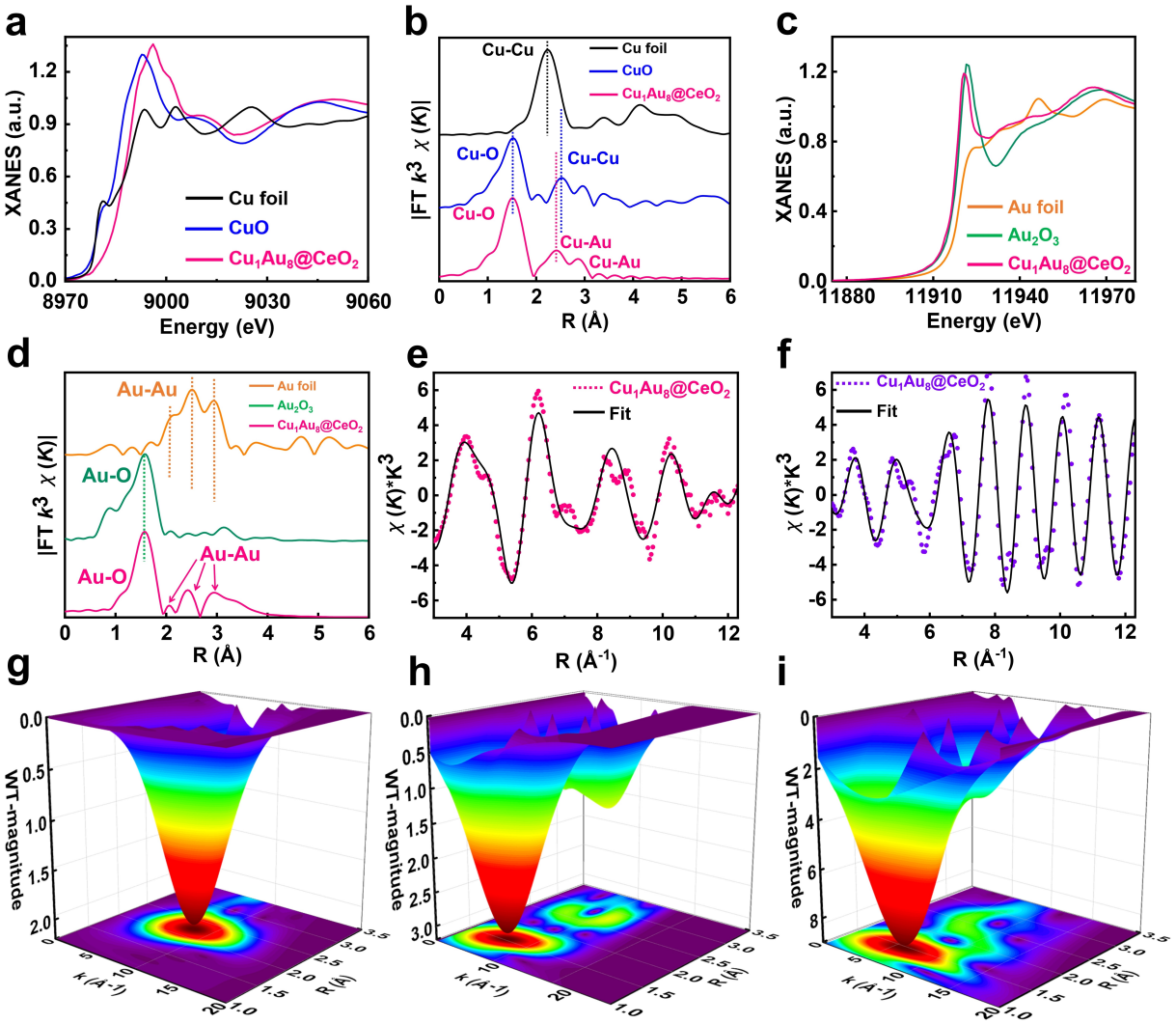

Figure 2. a) The Cu K-edge XANES spectra. b) Fourier transform extended X-ray absorption fine structure (FT-EXAFS) spectra of samples. c) The Au L_3-edge XANES spectra of samples. d) FT-EXAFS spectra of samples. e,f) EXAFS fitting plots of $Cu_1Au_8@CeO_2$. g–i) Wavelet transform (WT)-EXAFS plots of Cu foil, CuO, and $Cu_1Au_8@CeO_2$.

voltammetry (LSV) tests were performed to evaluate electrochemical activity of $Cu_1Au_8@CeO_2$ (Figure 3a). Notably, current density over $Cu_1Au_8@CeO_2$ in Ar-saturated 0.1 M KNO_3 is higher than that in Ar-saturated 0.1 M K_2SO_4, implying NO_3^- reduction reactions may occur. Current density over $Cu_1Au_8@CeO_2$ in CO_2-saturated 0.1 M KNO_3 is higher than that in Ar-saturated 0.1 M KNO_3, demonstrating synergistic reduction reaction of C-species and N- species, which is beneficial for subsequent C–N coupling. Meanwhile, $Cu_1Au_8@CeO_2$ exhibits the highest total current densities among reference catalysts (Figure S7), attributed to its unique atomic regulation and interfacial interaction.

Urea electrosynthesis was performed under ambient conditions. Its concentration was quantified by ultraviolet-visible spectroscopy (UV/Vis, diacetyl monoxime method) (Figure S8).[4,5,23] Urea yield rates and FEs were investigated in CO_2-saturated 0.1 M KNO_3 within a potential range from −0.54 to −1.04 V vs. RHE (Figure 3b–c). $Cu_1Au_8@CeO_2$ displayed the highest urea yield rate (813.6 $\mu g\,h^{-1}\,mg_{cat}^{-1}$ at −0.94 V vs. RHE) and FE (45.2 % at −0.74 V vs. RHE) among those samples. $Cu@CeO_2$, $Au@CeO_2$, and CeO_2 exhibited the highest urea FEs of 18.8 % (−0.94 V vs. RHE), 11.5 % (−0.94 V vs. RHE) and 4.1 % (−0.85 V vs. RHE) respectively. Urea yield rates and FEs of $Cu_1Au_8@CeO_2$ decreased after −1.04 V vs. RHE, primarily due to competitive hydrogen evolution reaction (HER) was gradually gaining ground. FEs and yield rates for urea in this work are compared with those of previous works (Table S2), it indicates $Cu_1Au_8@CeO_2$ catalyst has favorable activity and yield rate simultaneously. To explore the effect of Cu/Au ratio on electrocatalytic performance, a series reference catalysts ($Cu_xAu_y@CeO_2$) were synthesized. These catalysts are denoted as $Cu_1Au_1@CeO_2$, $Cu_1Au_5@CeO_2$, and $Cu_1Au_{14}@CeO_2$, based on the results of ICP-AES. TEM images and XRD patterns (Figure S9–S10) confirm successful loading of CuAu NPs onto CeO_2 nanorods. Electrochemical performances were then investigated (Figure S11).

© 2024 Wiley-VCH GmbH

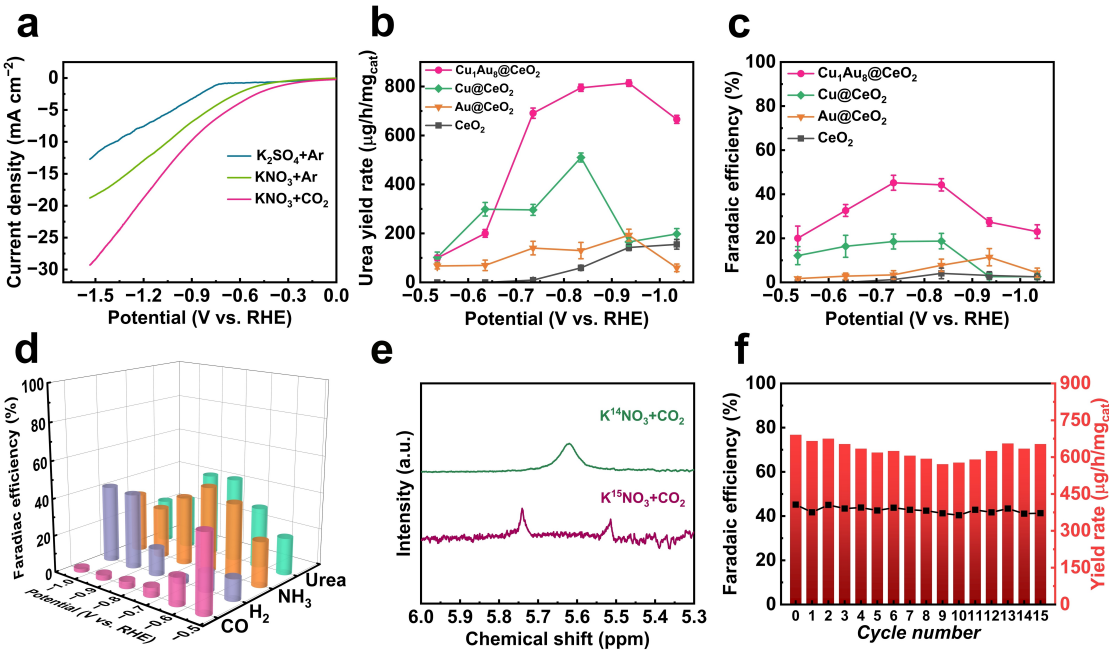

Figure 3. a) LSV curves over Cu_1Au_8@CeO_2 catalyst in different electrolytes. b) Yield rates of urea for Cu_1Au_8@CeO_2 and reference catalysts. c) Faradaic efficiencies of urea for Cu_1Au_8@CeO_2 and reference catalysts. d) Faradaic efficiencies for all products over Cu_1Au_8@CeO_2 catalyst. e) ^{1}H NMR spectra of electrolytes after electrolysis in 0.1 M ^{15}N- and ^{14}N-labeled KNO_3. f) The durability of Cu_1Au_8@CeO_2 for urea production at −0.74 V vs. RHE.

As the Cu/Au ratio decreased, the urea yield rates and FEs increased. The maximum was achieved at a ratio of 1:8 attributed to CuAu SAA formation. Further reduction in the ratio led to a decrease in FE and yield rate, probably due to a decrease of single-atom Cu active sites.

Other potential by-products, including ammonia (NH_3), hydrazine (N_2H_4), C_1 products, and C_2 products were investigated (Figure 3d and S12). NH_3, CO, and H_2 were detected as by-products, indicating Cu_1Au_8@CeO_2 exhibits excellent activity for both CO_2RR and NO_3RR, which is a prerequisite for efficient C–N coupling. NH_3 yield rates and FEs are illuminated in Figure S13. The highest NH_3 yield rate over Cu_1Au_8@CeO_2 reached 484.3 μg h^{-1} mg$_{cat}$$^{-1}$ at −0.84 V vs. RHE, the FE of NH_3 was up to 36.9 %. The total [N] Faraday efficiency was evaluated to reach 91.1 % at −0.74 V vs. RHE (Figure S14), and the total Faradaic efficiencies for all products exceeded 97 %, subsequent product analyses of relevant reactions over Cu@CeO_2, Au@CeO_2, and CeO_2 are shown in Figure S15. Current densities for urea production (j_{urea}) over Cu_1Au_8@CeO_2, Cu@CeO_2, Au@CeO_2, and CeO_2 are presented in Figure S16. At each applied potential, j_{urea} over Cu_1Au_8@CeO_2 was higher than those of other reference samples, suggesting isolated Cu sites and EMSI effect between SAA and CeO_2 can simultaneously promoting electrocatalytic performance.

To identify nitrogen source in urea production, isotope labeling experiments were performed by using $^{15}NO_3^-$ as the N source at −0.94 V vs. RHE. In Figure 3e, the signals of ^{15}N-labeled $^{15}NH_2CO^{15}NH_2$ exhibit two typical peaks at 5.73 and 5.50 ppm, in contrast to the single peak of $^{14}NH_2CO^{14}NH_2$ at 5.62 ppm, confirming nitrate ions in the electrolyte serve as the N source in urea production.[5] Meanwhile, no urea was detected neither in CO_2-saturated K_2SO_4 electrolyte or Ar-saturated KNO_3 electrolyte, further confirming the produced urea is not from foreign impurities.

To investigate the durability of Cu_1Au_8@CeO_2 toward urea production, consecutive test cycles were performed at −0.74 V and −0.94 V vs. RHE (Figure 3f and S17), respectively. Each test involves a 2-hour reaction. After each test, the electrode was treated instantly with deionized water and vacuum drying. After recycling at −0.74 V vs. RHE for 15 times, the final FE and yield rate of urea remained 41.3 % and 653.2 μg h^{-1} mg$_{cat}$$^{-1}$, respectively. It decreased slightly compared with the initial the FE of 45.2 % and yield rate of 690.9 μg h^{-1} mg$_{cat}$$^{-1}$, attributed to the exfoliation of electrocatalysts from electrode surface.[24] The performance of the recycled Cu_1Au_8@CeO_2 catalyst at −0.94 V vs. RHE also remains stable. Additionally, no appreciable morphology and crystal structure changes were observed for the recycled Cu_1Au_8@CeO_2 (Figure S18–S20). These findings prove satisfactory stability of the electrocatalyst.

Electrochemical impedance spectroscopy (EIS) was conducted to analyze kinetic properties of electrocatalysts (Figure S21a). Compared with CeO_2 and Au@CeO_2, Cu_1Au_8@CeO_2 exhibited the smallest charge-transfer resistance (R_{ct}), indicating the introduction of single-atom Cu sites and EMSI between SAA and CeO_2 can reduce charge transfer barrier during the reaction. To examine electrochemical active surface area (ECSA), the electrochemical double-layer capacitance (C_{dl}) of Cu_1Au_8@CeO_2, Au@CeO_2, and CeO_2 were measured (Figure S21b). The ECSA for Cu_1Au_8@CeO_2 was larger than those of CeO_2 and Au@-

 © 2024 Wiley-VCH GmbH

CeO_2, suggesting the atomic dispersion of Cu in $Cu_1Au_8@CeO_2$ enhances intrinsic activity.

In situ Raman spectroscopy was then conducted to track surface-adsorbed intermediates during the reaction (Figure S22). At open circuit potential (OCP) in Figure 4a, peaks at 459 and 600 cm^{-1} represented CeO_2 and Cu oxides, while adsorbed species of NO_3^- appeared at 1045 cm^{-1}.[25] The Cu oxide peak decreased with negative potentials, confirming the reduction of CuO to Cu_2O.[19] Surface Cu–CO species (280 and 381 cm^{-1}) intensified with higher potentials, promoting C–N coupling and urea production.[26] NO_3^- reduction intermediates manifested at 797, 1089, 1444, and 1581 cm^{-1}, corresponding to the bending vibration of NO_2^- (δNO_2^-), symmetrical vibration of NO_2^- ($\nu_s NO_2^-$), symmetrical bending vibration of NH_3^+ ($\delta_s NH_3^+$), and $\delta_{as}NH_2$ of NH_3, respectively. Additionally, δ(CN) and ν_s(CN) bonds appeared at 565 and 1024 cm^{-1}, indicating urea formation.[27]

In situ Fourier transform infrared spectroscopy (FTIR) was performed over $Cu_1Au_8@CeO_2$ to monitor the bonding structure of intermediate species. In Figure 4a, infrared signals were collected from 1000 to 4000 cm^{-1} within the potential range from −0.54 V to −1.04 V vs. RHE. There are infrared bands situating at 2917,1625 and 1171 cm^{-1},

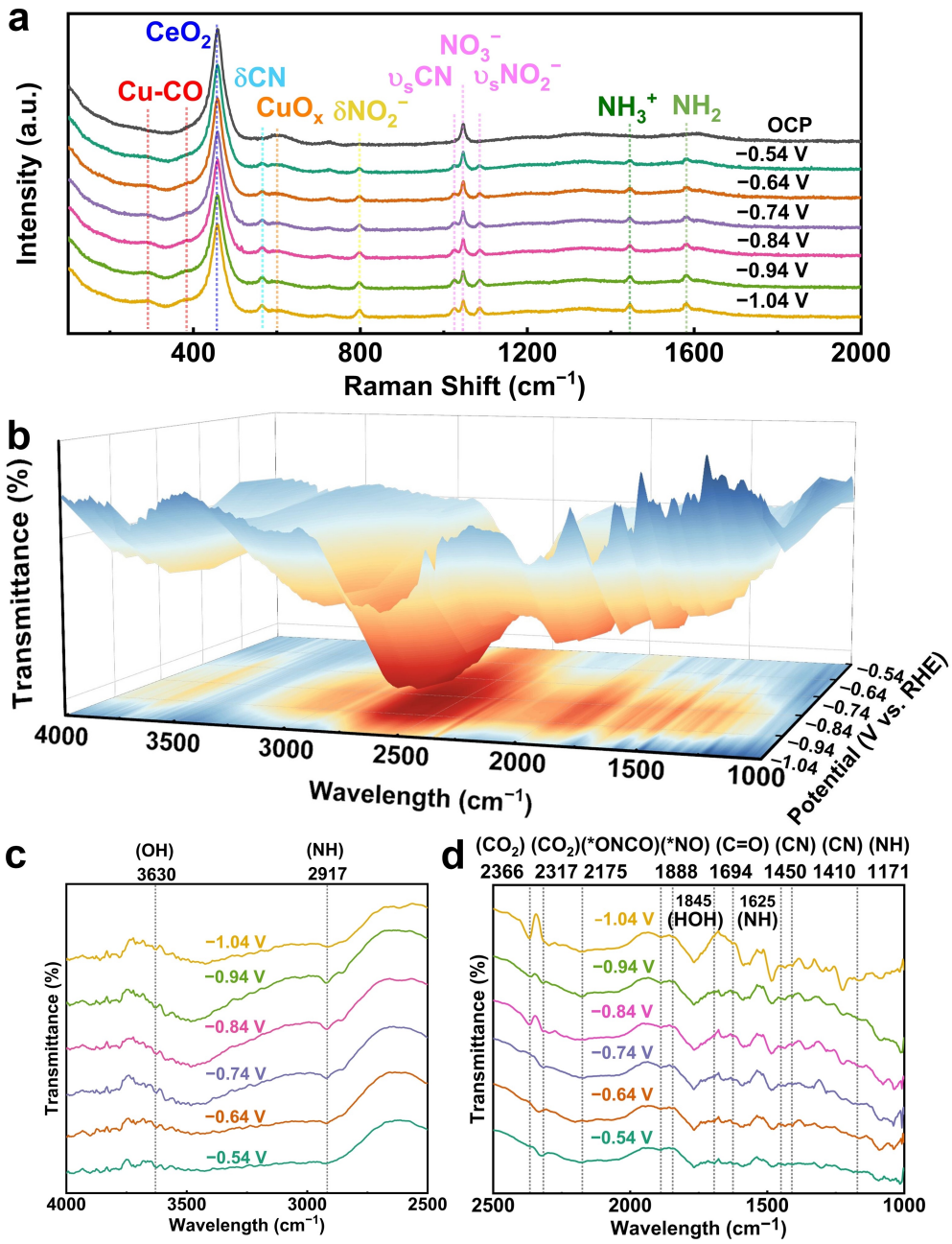

Figure 4. a) In situ Raman spectra of $Cu_1Au_8@CeO_2$ at different potentials. b) Three-dimensional in situ FTIR spectra in the range of 1000–4000 cm^{-1}. Infrared signal in the range of c) 2500–4000 cm^{-1} and d) 1000–2500 cm^{-1} under various potentials over $Cu_1Au_8@CeO_2$.

© 2024 Wiley-VCH GmbH

corresponding to the stretching, bending, and rocking modes of $-NH_2$ in urea.[28] The peak at 1888 cm^{-1} is assigned to the accumulation of *NO,[29] suggesting the moderated adsorption of *NO on $Cu_1Au_8@CeO_2$. The band at 1694 cm^{-1} can be assigned to C=O,[30] implying the formation of *CO intermediate species. The characteristic peak at 2175 cm^{-1} is assigned to *ONCO intermediate species, implying subsequent C–N coupling process.[18] The band at 1450 cm^{-1} is attributed to the C–N stretching of free urea.[31] Meantime, the stretching mode of C–N can also be observed at 1410 cm^{-1}, demonstrating a part of urea can be coordinated with electrocatalysts.[32] On this basis, we hypothesize that the coupling of *NO with *CO plays a pivotal role in the first C–N bond formation of *ONCO and is conducive to urea production. Besides, peaks at about 1845, 2317, and 2366 cm^{-1} originated from water HOH bending, adsorbed CO_2, and residual gaseous CO_2, respectively.[18] The relative intensity of *ONCO varied with applied potentials, reaching its maximum at −0.94 V vs. RHE, consistent with the change in urea yield rates with charged potentials. This insight into urea synthesis mechanisms confirms the generation of *ONCO intermediate is a crucial step in urea production, and atomically dispersed Cu atoms in $Cu_1Au_8@CeO_2$ catalyst remarkably stabilize these intermediates, promoting C–N coupling and enhancing urea selectivity.

Density functional theory (DFT) calculations were further investigated to elucidate the mechanism of C–N coupling and parallel proton-coupling electron-transfer (PCET) processes (Figure S23–S25). Projected density of states (PDOS) plots in Figure S26 indicate higher-energy distribution of Au 5d states in $CuAu@CeO_2$ above the Fermi level, granting surface Au sites a stronger bonding ability for *ONCO intermediate stabilization.[33] In Figure 5a and Figure S27, energy barriers for C–N coupling of four N-containing intermediates are lower than those for corresponding hydrogenation reactions with $Cu_1Au_8@CeO_2$ serving as the catalyst, indicating kinetic favorability of C–N coupling on $Cu_1Au_8@CeO_2$ catalyst. Notably, a mere 0.17 eV energy barrier is required to initiate the coupling reaction of *NO with *CO, suggesting a preference for *OCNO formation over $*OCNH_2$ (1.14 eV), *OCNH (1.21 eV), or *OCN (1.55 eV). Conversely, energy barrier for the coupling reaction of *NO with *CO on $Au@CeO_2$ catalyst is higher at 0.51 eV (Figure 5b). Additionally, energy barriers for hydrogenation reactions over $Au@CeO_2$ catalyst remain higher than those for C–N coupling of four N-containing intermediates, affirming $Au@CeO_2$ catalyst shares the same catalytic pathway for C–N coupling as $Cu_1Au_8@CeO_2$ catalyst.

Reaction energy paths for all steps on $Cu_1Au_8@CeO_2$ and $Au@CeO_2$ are shown in Figure 5c and Figure S28. Corresponding atomic configurations of each step on electrocatalysts are illustrated in Figure S29 and S30. Urea synthesis over $Cu_1Au_8@CeO_2$ starts with thermodynamically spontaneous reduction of NO_3^- to $*NO_2$ intermediate. The surface of electrocatalysts is fully covered by $*NO_2$ to inhibit excessive CO_2 reduction. Subsequently, the hydrogenation of $*CO_2$ and $*NO_2$ on $Cu_1Au_8@CeO_2$ go uphill with free energies of 0.28 eV and 0.37 eV, respectively. As a contrast,

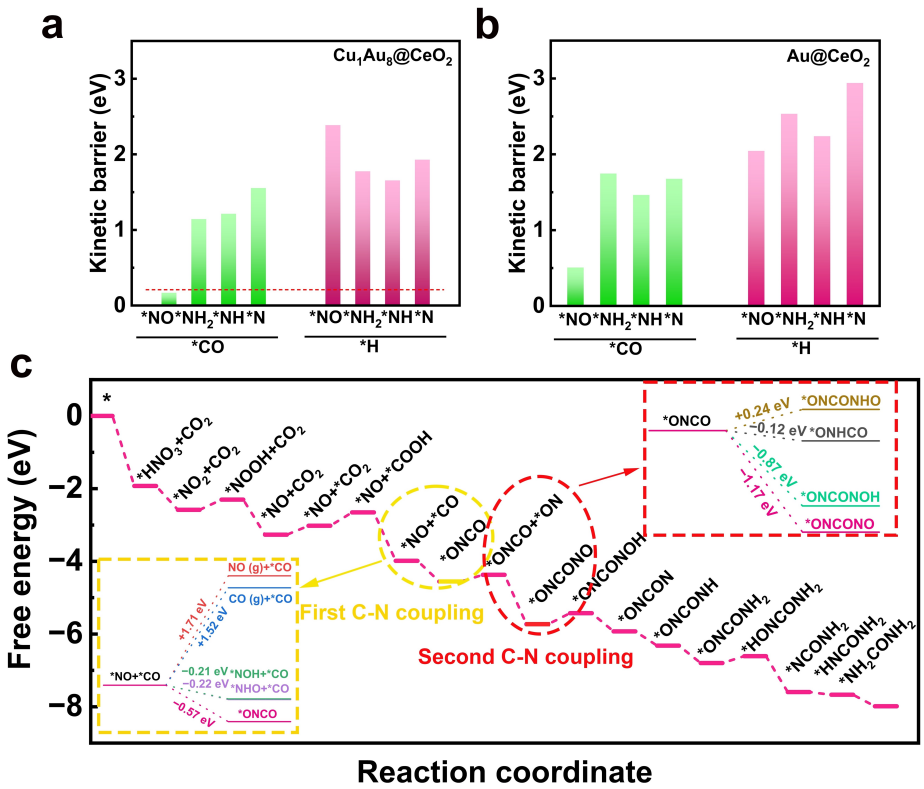

Figure 5. Comparison of coupling energy barrier for *NO, *N, *NH, and $*NH_2$ with *CO and protonation, on a) $Cu_1Au_8@CeO_2$ and b) $Au@CeO_2$ catalyst. c) Free-energy diagram for urea production over $Cu_1Au_8@CeO_2$, insets are potential states for the first and second C–N coupling paths.

© 2024 Wiley-VCH GmbH

the hydrogenation of $*CO_2$ and $*NO_2$ on $Au@CeO_2$ are 0.49 eV and 0.42 eV, which are higher than those of $Cu_1Au_8@CeO_2$, indicating adsorption behaviors of intermediate species can be significantly modulated by the introduction of single-atom Cu sites. Noted that as *CO forms, the combination of *NO and *CO is more favorable, leading to the formation of *ONCO intermediate via Eley-Rideal (ER) mechanism,[34] with an energy barrier of −0.57 eV. This contrasts with the reduction to *NHO (−0.22 eV), *NOH (−0.21 eV), or CO (g, −1.52 eV), NO (g, −1.71 eV) intermediates (Figure S20 and Figure S22a). In the second C–N coupling, only an energy barrier of −1.17 eV is required to overcome in the coupling reaction of *ONCO with *NO, indicating a propensity for *ONCONO formation over *ONCONHO (0.24 eV), *ONCONOH (−0.87 eV), or *ONHCO (−0.12 eV) (Figure S21 and Figure S22b). Thereafter, *ONCONO intermediate species are reduced to urea through eight electro-proton-transfer steps. Subsequent multiple electro-coupled-proton transfer processes are exothermic until the formation of $*HONCONH_2$. The above results indicate urea formation is thermodynamically and kinetically preferred on $Cu_1Au_8@CeO_2$, which is consistent with experimental observations.

Conclusions

In this work, $Cu_1Au_8@CeO_2$ with EMSI effect has been reported as an efficient electrocatalyst for co-reduction of NO_3^- and CO_2 to synthesize urea. The resultant $Cu_1Au_8@CeO_2$ achieved a high urea yield rate of 813.6 $\mu g\,h^{-1}\,mg_{cat}^{-1}$ at −0.94 V vs. RHE and a urea FE of 45.2 % at −0.74 V vs. RHE. Furthermore, in situ experiments and theoretical calculations indicate single-atom Cu sites can regulate the adsorption behavior of intermediate species. Cu–Au bimetallic sites synergistically promote the formation of C–N bond through spontaneous coupling of *CO and *NO to generate the key intermediate of *ONCO. More importantly, EMSI between CuAu SAA and CeO_2 carrier further modulate electron structure, endowing electrocatalysts with superior activity and durability. This work fabricates SAA electrocatalysts with EMSI effect to tailor C–N coupling at the atomic level, and the findings are expected to guide the development of C–N coupling systems in the future.

Acknowledgements

The authors acknowledge financial support from the National Natural Science Foundation of China (Grant No. 22303004, 22278023, 22208010), Beijing Municipal Science and Technology Planning Project (Z221100002722002), Beijing Natural Science Foundation (2222015).

Conflict of Interest

The authors declare no conflict of interest.

Data Availability Statement

The data that support the findings of this study are available from the corresponding author upon reasonable request.

Keywords: C–N coupling · Carbon dioxide · Electrosynthesis · Nitrate · Urea

[1] D. McKie, *Nature* **1944**, *153*, 608–610.
[2] J. Li, Y. Zhang, K. Kuruvinashetti, N. Kornienko, *Nat. Chem. Rev.* **2022**, *6*, 303–319.
[3] R. Lan, S. Tao, J. T. S. Irvine, *Energy Environ. Sci.* **2010**, *3*, 438–441.
[4] X. Zhang, X. Zhu, S. Bo, C. Chen, M. Qiu, X. Wei, N. He, C. Xie, W. Chen, J. Zheng, P. Chen, S. P. Jiang, Y. Li, Q. Liu, S. Wang, *Nat. Commun.* **2022**, *13*, 5337.
[5] C. Lv, L. Zhong, H. Liu, Z. Fang, C. Yan, M. Chen, Y. Kong, C. Lee, D. Liu, S. Li, J. Liu, L. Song, G. Chen, Q. Yan, G. Yu, *Nat. Sustain.* **2021**, *4*, 868–876.
[6] N. N. Meng, X. M. Ma, C. H. Wang, Y. T. Wang, R. Yang, J. Shao, Y. M. Huang, Y. Xu, B. Zhang, Y. F. Yu, *ACS Nano* **2022**, *16*, 9095–9104.
[7] Y. Zhao, Y. Ding, W. Li, C. Liu, Y. Li, Z. Zhao, Y. Shan, F. Li, L. Sun, F. Li, *Nat. Commun.* **2023**, *14*, 4491.
[8] Y. Wang, S. Xia, R. Cai, J. Zhang, C. Yu, J. Cui, Y. Zhang, J. Wu, Y. Wu, *Angew. Chem. Int. Ed.* **2024**, e202318589.
[9] S. Shin, S. Sultan, Z.-X. Chen, H. Lee, H. Choi, T.-U. Wi, C. Park, T. Kim, C. Lee, J. Jeong, H. Shin, T.-H. Kim, H. Ju, H. C. Yoon, H.-K. Song, H.-W. Lee, M.-J. Cheng, Y. Kwon, *Energy Environ. Sci.* **2023**, *16*, 2003–2013.
[10] M. Sun, G. Wu, J. Jiang, Y. Yang, A. Du, L. Dai, X. Mao, Q. Qin, *Angew. Chem. Int. Ed.* **2023**, *62*, e202301957.
[11] C. T. Campbell, *Nat. Chem.* **2012**, *4*, 597–598.
[12] Y. Cao, S. Chen, S. Bo, W. Fan, J. Li, C. Jia, Z. Zhou, Q. Liu, L. Zheng, F. Zhang, *Angew. Chem. Int. Ed.* **2023**, *62*, e202303048.
[13] R. T. Hannagan, G. Giannakakis, M. Flytzani-Stephanopoulos, E. C. H. Sykes, *Chem. Rev.* **2020**, *120*, 12044–12088.
[14] G. Kyriakou, M. B. Boucher, A. D. Jewell, E. A. Lewis, T. J. Lawton, A. E. Baber, H. L. Tierney, M. Flytzani-Stephanopoulos, E. C. H. Sykes, *Science* **2012**, *335*, 1209–1212.
[15] M. T. Greiner, T. E. Jones, S. Beeg, L. Zwiener, M. Scherzer, F. Girgsdies, S. Piccinin, M. Armbrüster, A. Knop-Gericke, R. Schlögl, *Nat. Chem.* **2018**, *10*, 1008–1015.
[16] P. Zhan, S. Yang, L. Huang, X. Zhang, X. Li, L. Lu, P. Qin, *Langmuir* **2023**, *39*, 8306–8313.
[17] C. Chen, X. Zhu, X. Wen, Y. Zhou, L. Zhou, H. Li, L. Tao, Q. Li, S. Du, T. Liu, D. Yan, C. Xie, Y. Zou, Y. Wang, R. Chen, J. Huo, Y. Li, J. Cheng, H. Su, X. Zhao, W. Cheng, Q. Liu, H. Lin, J. Luo, J. Chen, M. Dong, K. Cheng, C. Li, S. Wang, *Nat. Chem.* **2020**, *12*, 717–724.
[18] X. Wei, X. Wen, Y. Liu, C. Chen, C. Xie, D. Wang, M. Qiu, N. He, P. Zhou, W. Chen, J. Cheng, H. Lin, J. Jia, X.-Z. Fu, S. Wang, *J. Am. Chem. Soc.* **2022**, *144*, 11530–11535.
[19] M. Wang, H. Chen, M. Wang, J. Wang, Y. Tuo, W. Li, S. Zhou, L. Kong, G. Liu, L. Jiang, G. Wang, *Angew. Chem. Int. Ed.* **2023**, *62*, e202306456.
[20] L.-P. Yuan, W.-J. Jiang, X.-L. Liu, Y.-H. He, C. He, T. Tang, J. Zhang, J.-S. Hu, *ACS Catal.* **2020**, *10*, 13227–13235.
[21] W. Zhang, J. Chang, G. Wang, Z. Li, M. Wang, Y. Zhu, B. Li, H. Zhou, G. Wang, M. Gu, Z. Feng, Y. Yang, *Energy Environ. Sci.* **2022**, *15*, 1573–1584.
[22] X. Liu, C. Ao, X. Shen, L. Wang, S. Wang, L. Cao, Z. Wei, J. Dong, J. Bao, T. Ding, L. Zhang, T. Yao, *Nano Lett.* **2020**, *20*, 8319–8325.

© 2024 Wiley-VCH GmbH

[23] Y. Feng, H. Yang, Y. Zhang, X. Huang, L. Li, T. Cheng, Q. Shao, *Nano Lett.* **2020**, *20*, 8282–8289.
[24] P. Zhan, X. Liu, S. Zhang, Q. Zhu, H. Zhao, C. Ren, J. Zhang, L. Lu, D. Cai, P. Qin, *ACS Appl. Mater. Interfaces* **2023**, *15*, 12855–12863.
[25] S. Loridant, *Catal. Today* **2021**, *373*, 98–111.
[26] Z. Wang, Y. Li, X. Zhao, S. Chen, Q. Nian, X. Luo, J. Fan, D. Ruan, B.-Q. Xiong, X. Ren, *J. Am. Chem. Soc.* **2023**, *145*, 6339–6348.
[27] Y. Wang, S. Xia, J. Zhang, Z. Li, R. Cai, C. Yu, Y. Zhang, J. Wu, Y. Wu, *ACS Energy Lett.* **2023**, *8*, 3373–3380.
[28] R. Keuleers, H. O. Desseyn, B. Rousseau, C. Van Alsenoy, *J. Phys. Chem.* **1999**, *103*, 4621–4630.
[29] K. I. Hadjiivanov, *Catal. Rev. Sci. Eng.* **2000**, *42*, 71–144.
[30] J. B. Bossa, P. Theulé, F. Duvernay, F. Borget, T. Chiavassa, *Astron. Astrophys.* **2008**, *492*, 719–724.
[31] Y. Yao, S. Zhu, H. Wang, H. Li, M. Shao, *J. Am. Chem. Soc.* **2018**, *140*, 1496–1501.
[32] J. Geng, S. Ji, M. Jin, C. Zhang, M. Xu, G. Wang, C. Liang, H. Zhang, *Angew. Chem. Int. Ed.* **2023**, *62*, e202210958.
[33] J. Qin, N. Liu, L. Chen, K. Wu, Q. Zhao, B. Liu, Z. Ye, *ACS Sustainable Chem. Eng.* **2022**, *10*, 15869–15875.
[34] X. Wei, Y. Liu, X. Zhu, S. Bo, L. Xiao, C. Chen, T. T. T. Nga, Y. He, M. Qiu, C. Xie, D. Wang, Q. Liu, F. Dong, C.-L. Dong, X.-Z. Fu, S. Wang, *Adv. Mater.* **2023**, *35*, 2300020.

Manuscript received: May 13, 2024
Accepted manuscript online: May 24, 2024
Version of record online: July 9, 2024

© 2024 Wiley-VCH GmbH